Oncology
and Radiotherapy©
20(4) 2026 : 001-009 • RESEARCH ARTICLE

Development and Radiological Validation of a Low-Cost Anthropomorphic Orbital Phantom for CT Dosimetry and Radiation Therapy Applications

Walid Allioui[1,2,3]*, Abdellah khallouqi[1], Hamza Sekkat[1], A. Slimani[1], Abdellah halimi[1], Omar El rhazouani[1]

[1]Laboratory of Health Sciences and Technologies, Higher Institute of Health Sciences, Hassan 1st University, Settat, Morocco
[2]Higher Institute of Nursing Professions and Health Techniques (ISPITS), Ministry of Health and Social Protection, Marrakech, Morocco
[3]Dar Seha Center of Radiology and Medical Imaging, Marrakech, Morocco

ABSTRACT

This study aimed to develop and characterize a low-cost anthropomorphic orbital phantom based on epoxy resin tissue-equivalent materials for computed tomography (CT) and radiation therapy applications. The phantom incorporated four main orbital structures, including orbital bone, extraocular muscles, optic nerve, and crystalline lens, using optimized epoxy-based composite formulations. Radiological characterization was performed through effective atomic number, electron density, mass attenuation coefficient, and CT number analyses over energy ranges extending from 10KeV to 25 MeV. In the diagnostic energy range (60–200 keV), the average deviations in mass attenuation coefficients were approximately −1.2% for orbital bone, +1.6% for the crystalline lens, −0.2% for extraocular muscle, and −0.3% for the optic nerve. At high energies (200 keV–25 MeV), the average deviations remained low, with values of approximately −1.6%, +0.09%, −1.0%, and −1.1% for bone, lens, muscle, and optic nerve, respectively. The experimentally measured CT numbers also showed close agreement with the corresponding human tissues, with values of 601.1±60 HU for bone, 36.0±2.1 HU for muscle, 34.7±2.0 HU for optic nerve, and 65.2±6.8 HU for the crystalline lens. These results confirm the suitability of the developed materials for reproducing the attenuation and radiation interaction properties of orbital tissues under both diagnostic and therapeutic conditions.

Keywords: Radiation therapy; Computed tomography; Anthropomorphic phantom; Tissue-equivalent materials; Epoxy resin

Address for correspondence:
Walid Allioui,
Laboratory of Health Sciences and Technologies,
Higher Institute of Health Sciences, Hassan 1st University, Settat, Morocco,
E-mail: w.allioui@uhp.ac.ma

Word count: 4062 **Figure:** 4 **Table:** 2 **References:** 45

Received: 01 April, 2026, Manuscript No. OAR-26-189449;
Editor assigned: 04 April, 2026, PreQC No. OAR-26-189449 (PQ);
Reviewed: 21 April, 2026, QC No. OAR-26-189449;
Revised: 27 April, 2026, Manuscript No. OAR-26-189449 (R);
Published: 30 April, 2026

INTRODUCTION

Orbital and peri-orbital tumors represent a major clinical challenge in radiation therapy because of the anatomical complexity of the orbital region and the close proximity of highly radiosensitive critical structures such as the lens, optic nerve, extraocular muscles, and craniofacial bones [1]. Modern radiotherapy techniques, including conformal radiotherapy, intensity-modulated radiation therapy (IMRT), volumetric modulated arc therapy (VMAT), and proton therapy, have significantly improved dose conformity and tumor control [2,3]. Nevertheless, despite these technological advances, unintended irradiation of healthy orbital tissues remains a critical issue that may lead to severe complications, including radiation-induced cataracts [4], optic neuropathy [5], ocular motility disorders [6], and post-radiation bone damage [7]. Consequently, accurate dosimetric optimization and experimental validation of treatment plans require anthropomorphic tools capable of realistically reproducing both the anatomical and radiological properties of human orbital tissues [8–10]. Anthropomorphic phantoms are useful in medical physics and radiation therapy because they enable controlled and reproducible investigations without additional radiation exposure to patients [11,12]. They are widely used for treatment planning system verification, evaluation of advanced irradiation techniques, Monte Carlo validation, and quality assurance procedures [13,14]. However, currently available commercial phantoms present several limitations. First, their high cost considerably restricts accessibility in many hospitals [15,16]. Second, the materials used in these phantoms do not always accurately reproduce the radiological behavior of human tissues [17,18], particularly in heterogeneous anatomical regions such as the orbit, where soft tissues, bony structures, and highly radiosensitive organs coexist within a limited volume. These discrepancies may lead to uncertainties in dose calculations and reduce the reliability of experimental validations in radiation therapy applications [19].

In recent years, substantial attention has been directed toward the development of tissue-equivalent materials for dosimetric and radiotherapeutic applications [20–23]. The radiological response of a material is not determined solely by its physical density, but also by key parameters such as mass attenuation coefficient, effective atomic number, and electron density. These parameters strongly

influence photon–matter interactions, including the photoelectric effect, Compton scattering, and pair production depending on the energy range involved [24–26]. Therefore, accurate reproduction of the electronic and atomic characteristics of biological tissues is essential to ensure realistic simulation of radiation transport and dose deposition in radiotherapy environments. Polymeric materials, particularly epoxy resin–based composites, have emerged as promising candidates for the fabrication of customized anthropomorphic phantoms [27–29]. Epoxy resin offers several advantages, including chemical stability, structural homogeneity, ease of fabrication, low production cost, and compatibility with complex anatomical molding techniques [30,31]. Moreover, its radiological properties can be modified through the incorporation of mineral or organic fillers to achieve characteristics close to those of targeted biological tissues [32,33]. Such an approach provides substantial flexibility for developing multi-tissue structures suitable for both imaging and radiation therapy applications. At the same time, advances in medical image segmentation and additive manufacturing have facilitated the development of anatomically realistic phantoms derived from patient imaging data. Three-dimensional printing technologies allow precise reproduction of the complex geometry of the human orbit, enabling simultaneous integration of bone and soft-tissue structures within a single anthropomorphic model [34–37]. This combination of anatomical realism and radiological tissue equivalence is particularly valuable for orbital dosimetry studies, where steep dose gradients may occur over very short anatomical distances. In this study, we present the development of a multi-tissue anthropomorphic orbital phantom dedicated to radiation therapy and dosimetric applications. The phantom incorporates several critical orbital structures, including orbital bone, extraocular muscles, optic nerve, and lens tissue, in order to reproduce the anatomical environment encountered in clinical practice. The developed materials were formulated using modified epoxy resin–based composites designed to approximate the radiological properties of the corresponding human tissues. A combined theoretical and experimental approach was employed to evaluate the materials in terms of mass attenuation coefficient, effective atomic number, electron density, and computed tomography response. The primary objective of this work is to provide a realistic, reproducible, and cost-effective anthropomorphic platform for dosimetric investigations in orbital radiation therapy. The developed phantom may be used for treatment planning system validation, assessment of dose distributions delivered to orbital organs at risk, optimization of advanced irradiation techniques, and radioprotection studies involving radiosensitive ocular structures. Furthermore, this approach offers significant potential for the development of patient-specific phantoms dedicated to precision radiotherapy and emerging applications in ocular and craniofacial oncology.

METHODS

Fabrication of the Anthropomorphic Orbital Phantom

Four orbital structures were considered in this study: the orbital bone, extraocular muscles, optic nerve, and crystalline lens. Different formulations were prepared according to the targeted tissue characteristics. The optic nerve–equivalent material was developed using a mixture composed of 92% epoxy resin and 8% acetone, whereas the material intended to reproduce the extraocular muscles was fabricated from pure epoxy resin. The lens-equivalent material was prepared by incorporating 7% sodium bicarbonate into a matrix containing 93% epoxy resin. For orbital bone simulation, a composite based on 55% epoxy resin and 45% calcium carbonate ($CaCO_3$) was developed. The anatomical geometry of the phantom was obtained from CT images of a 45-year-old patient weighing 75 kg acquired using a clinical scanner Philips access 16. The DICOM images were imported into 3D Slicer software for segmentation and three-dimensional reconstruction. Threshold-based segmentation was initially used for bone extraction, followed by manual refinement for the extraocular muscles, optic nerve, and crystalline lens. The reconstructed anatomical structures were exported in STL format and fabricated using fused deposition modeling (FDM) three-dimensional printing with PLA filament. The printed models served as master structures for mold fabrication. Silicone RTV-491 was then used to produce negative molds reproducing the orbital anatomy. Before casting, the prepared epoxy mixtures were manually degassed to reduce trapped air bubbles generated during mixing. After silicone curing, the PLA structures were removed, and the prepared epoxy-based tissue-equivalent materials were poured into the molds. Following polymerization and demolding, all fabricated orbital structures were positioned inside a cubic container and embedded within pure epoxy resin previously validated as a suitable soft tissue-equivalent material [38,39]. In addition, the internal air cavities of the phantom were filled using low-density polyurethane foam with a density of approximately 0.018 g/cm^3 to reproduce the radiological behavior of air-filled regions within the orbital anatomy [40]. The final assembly resulted in a complete anthropomorphic orbital phantom dedicated to computed tomography dosimetry and radiation therapy applications [Figure 1].

Elemental Composition Calculation

The elemental compositions of the developed composite materials

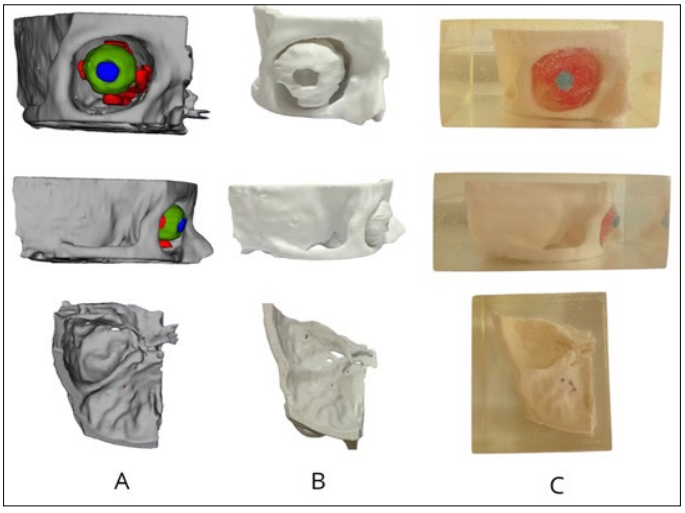

Figure 1: Orbital phantom fabrication process: **(A)** segmentation, **(B)** 3D printing, and **(C)** final anthropomorphic phantom.

were determined using a weighted mixture approach based on the mass fractions of each constituent component. For every material, the elemental weight fraction w_i of a given element i was calculated from the contributions of epoxy resin and incorporated additives according to the relation:

$$w_i = \sum_j f_i \, w_{ij} \quad (1)$$

Where f_j represents the mass fraction of constituent j in the composite material, and $w_{i,j}$ corresponds to the elemental weight fraction of element i in constituent j. The molecular compositions of epoxy resin ($C_{12}H_{25}ClO_5$), acetone (C_3H_6O), sodium bicarbonate ($NaHCO_3$), and calcium carbonate ($CaCO_3$) were used to determine the elemental proportions of hydrogen, carbon, oxygen, chlorine, sodium, and calcium in each developed formulation. The calculated elemental compositions were subsequently used as input data for theoretical calculations of the mass attenuation coefficient, effective atomic number, and electron density.

Effective Atomic Number and Electron Density Calculations

Following the determination of the elemental weight fractions [Table 1], the effective atomic number (Zeff) and electron density (ρe) of the developed tissue-equivalent materials were evaluated to investigate their radiological similarity to the corresponding human orbital tissues over a broad energy range. Theoretical calculations were performed using the Phy-X/PSD platforms [40] based on the elemental composition of each composite. The effective atomic number was calculated as an energy-dependent parameter describing the overall atomic behavior of the material during photon interactions [42], while the electron density was determined because of its important role in Compton scattering and radiation transport processes [43]. These parameters were evaluated over the energy range relevant to computed tomography and radiation therapy applications. The obtained Zeff and electron density values were subsequently compared with those of reference biological tissues [41] in order to assess the suitability of the developed materials for orbital dosimetry and radiotherapy applications.

Mass Attenuation Coefficient Calculation

The mass attenuation coefficients (μ/ρ) of the developed materials were evaluated to analyze their radiological behavior and tissue equivalence relative to the reference orbital tissues over a broad energy range (10 KeV, 25 MeV). Theoretical calculations were performed using the NIST XCOM database based on the elemental compositions and weight fractions of each composite material [44]. The mass attenuation coefficients were determined over an energy range covering both diagnostic and therapeutic domains in order to investigate photon–matter interactions under different energy conditions [45]. These calculations take into account the main interaction mechanisms, including the photoelectric effect, Compton scattering, and pair production. The obtained values for the developed tissue-equivalent materials were subsequently compared with those of the corresponding reference biological tissues to assess their suitability for computed tomography dosimetry and radiation therapy applications.

CT Number Evaluation

CT numbers were evaluated using the clinical imaging protocol in order to account for the polyenergetic nature of the X-ray beam as well as beam hardening effects, which may influence the radiological response of the developed materials. Indeed, photon–matter interactions and attenuation properties strongly depend on the effective energy of the incident beam, particularly in bone structures and materials containing elements with relatively high atomic numbers. Circular regions of interest (ROIs) were manually positioned within homogeneous regions of each material to measure the mean CT number expressed in Hounsfield Units (HU) together with the associated standard deviation. The measured HU values of the fabricated materials were subsequently compared with those of the corresponding human orbital tissues obtained from clinical images in order to evaluate the imaging equivalence of the developed composites for computed tomography dosimetry and radiation therapy applications.

RESULTS

This study aimed to develop tissue-equivalent materials capable of reproducing the radiological properties of the main orbital structures for computed tomography dosimetry and radiation therapy applications. Different epoxy-based formulations were prepared for the orbital bone, extraocular muscles, optic nerve, and crystalline lens using specific additives including acetone, $NaHCO_3$, and $CaCO_3$. The optic nerve–equivalent material composed of 92% epoxy resin and 8% acetone exhibited a density of approximately 1.16 g/cm³ compared with the reference optic nerve density of 1.039 g/cm³. The extraocular muscle–equivalent material fabricated from pure epoxy resin showed a density of approximately 1.20 g/cm³, while the reference muscle density was 1.05 g/cm³. The lens-equivalent material prepared from 93 % epoxy resin and 7% $NaHCO_3$ presented a density of approximately

Table 1: Elemental weight fractions of the reference biological tissues [41] and developed epoxy-based tissue-equivalent materials.

	H	C	N	O	Na	Mg	P	S	Cl	K	Ca
Skull	0.05	0.212	0.04	0.435	0.001	0.002	0.081	0.003	-	-	0.176
Epoxy-$CaCO_3$	0.058	0.371	-	0.351	-	-	-	-	-	-	0.14
Lens	0.096	0.195	0.057	0.646	0.001	-	0.001	0.003	0.001	-	-
Epoxy- $NaHCO_3$	0.084	0.481	-	0.301	0.019	-	-	-	0.115	-	-
muscle	0.102	0.143	0.034	0.71	0.001	-	0.002	0.003	0.001	0.004	-
Epoxy Resin	0.089	0.506	-	0.281	-	-	-	-	0.124	-	-
Optic Nerve	0.107	0.095	0.002	0.767	0.002	-	0.003	0.002	0.003	0.003	-
Epoxy–Acetone	0.09	0.515	-	0.281	-	-	-	-	0.114	-	-

1.25 g/cm³ relative to the reference lens density of 1.07 g/cm³. For orbital bone simulation, the composite composed of 55% epoxy resin and 45% $CaCO_3$ exhibited a density of approximately 1.49 g/cm³ compared with the reference bone density of 1.61 g/cm³. The Zeff results [Figure 2]. Showed that the largest deviations between the developed materials and the corresponding reference tissues were observed at low energies below 60 keV, where photon interactions are mainly dominated by the photoelectric effect and are therefore highly dependent on the atomic composition of the materials. In this low-energy region, the mean deviations were approximately –7.4% for the Epoxy–$CaCO_3$ bone-equivalent material, +43.7% for the Epoxy–$NaHCO_3$ lens-equivalent material, +33.8% for the muscle-equivalent epoxy resin, and +31.0% for the Epoxy–acetone optic nerve–equivalent material. In the diagnostic energy range between 60 and 200 keV, the differences progressively decreased for all investigated materials, indicating a closer radiological behavior relative to the reference orbital tissues. The average deviations in this region were approximately –9.5% for bone, +8.1% for lens, +7.1% for muscle, and +8.0% for the optic nerve. This behavior is mainly attributed to the increasing predominance of Compton scattering, which depends primarily on electron density rather than atomic number. At higher energies ranging from 200 keV to 25 MeV, the Zeff values of the developed composites remained relatively stable and followed trends close to those of the corresponding biological tissues. In this energy region, the mean deviations were approximately –9.1% for bone, +6.0% for lens, +4.8% for muscle, and +5.5% for the optic nerve, demonstrating the overall radiological equivalence of the fabricated materials for computed tomography dosimetry and radiation therapy applications.

The electron density analysis revealed a strong energy dependence for all developed tissue-equivalent materials [Figure 3]. In the low-energy region below 60 keV, the developed composites exhibited the largest deviations relative to the corresponding reference orbital tissues, mainly due to the significant influence of chemical composition and the electron concentration of the incorporated additives within the epoxy matrices. The average deviations observed in this region were approximately +4.9% for the Epoxy–$CaCO_3$ bone-equivalent material, +34.7% for the Epoxy–$NaHCO_3$ lens-equivalent material, +31.8% for the muscle-equivalent epoxy resin, and +15.8% for the Epoxy–acetone optic nerve–equivalent material. As the energy increased within the diagnostic range between 60 and 200 keV, the electron density curves of the developed materials progressively approached those of the corresponding biological tissues. In this region dominated by Compton scattering, the average deviations significantly decreased to approximately +0.04% for bone, +2.2% for the lens, +2.0% for muscle, and +0.8% for the optic nerve. This substantial reduction in the differences indicates a good electronic compatibility of the developed composites under clinical computed tomography energy conditions. Above 200 keV and up to 25 MeV, the electron density values remained relatively stable for all investigated materials. The

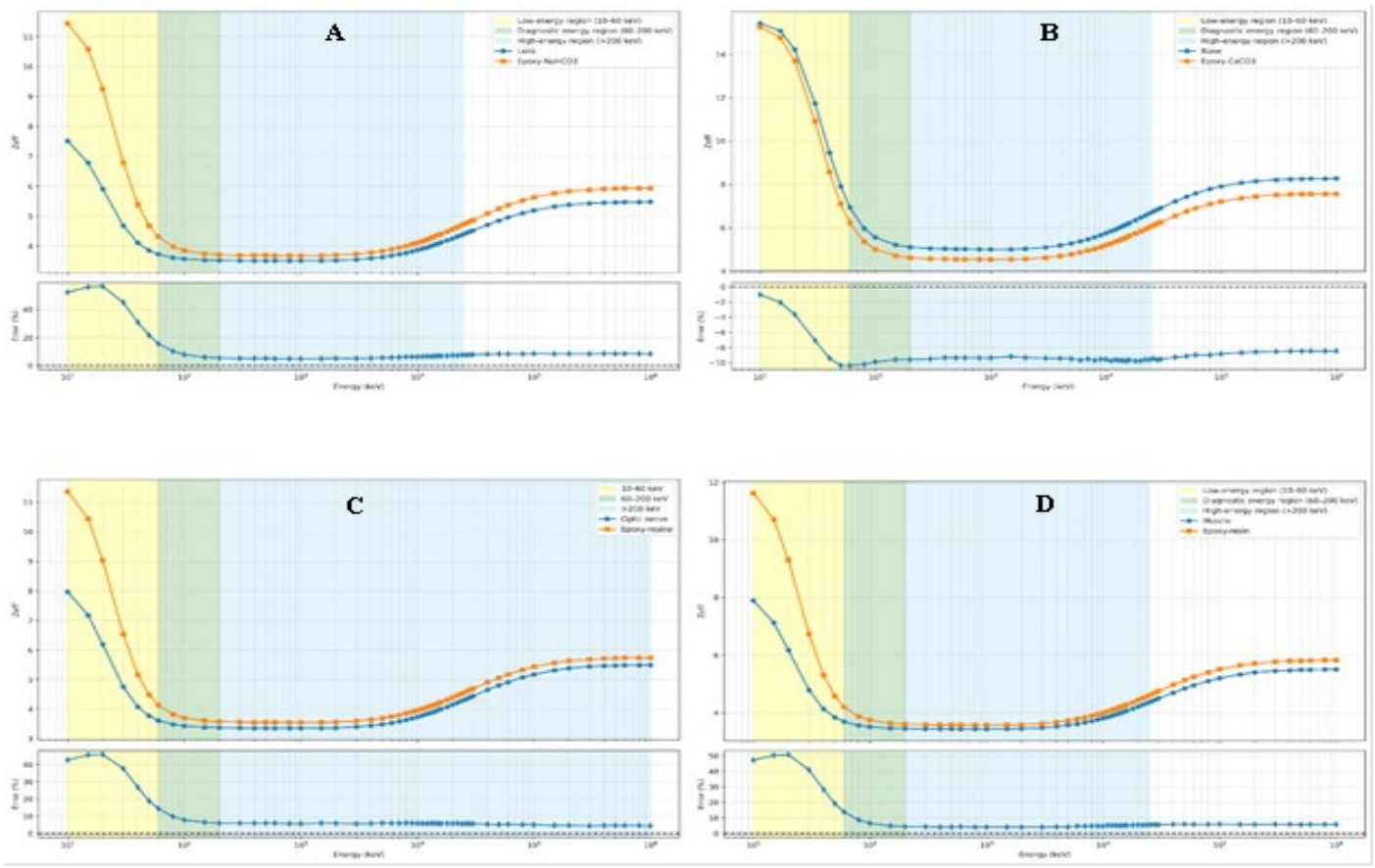

Figure 2: Energy-dependent effective atomic number (Zeff) comparison for (**A**) crystalline lens, (**B**) orbital bone, (**C**) optic nerve, and (**D**) Extraocular muscle tissue-equivalent materials.

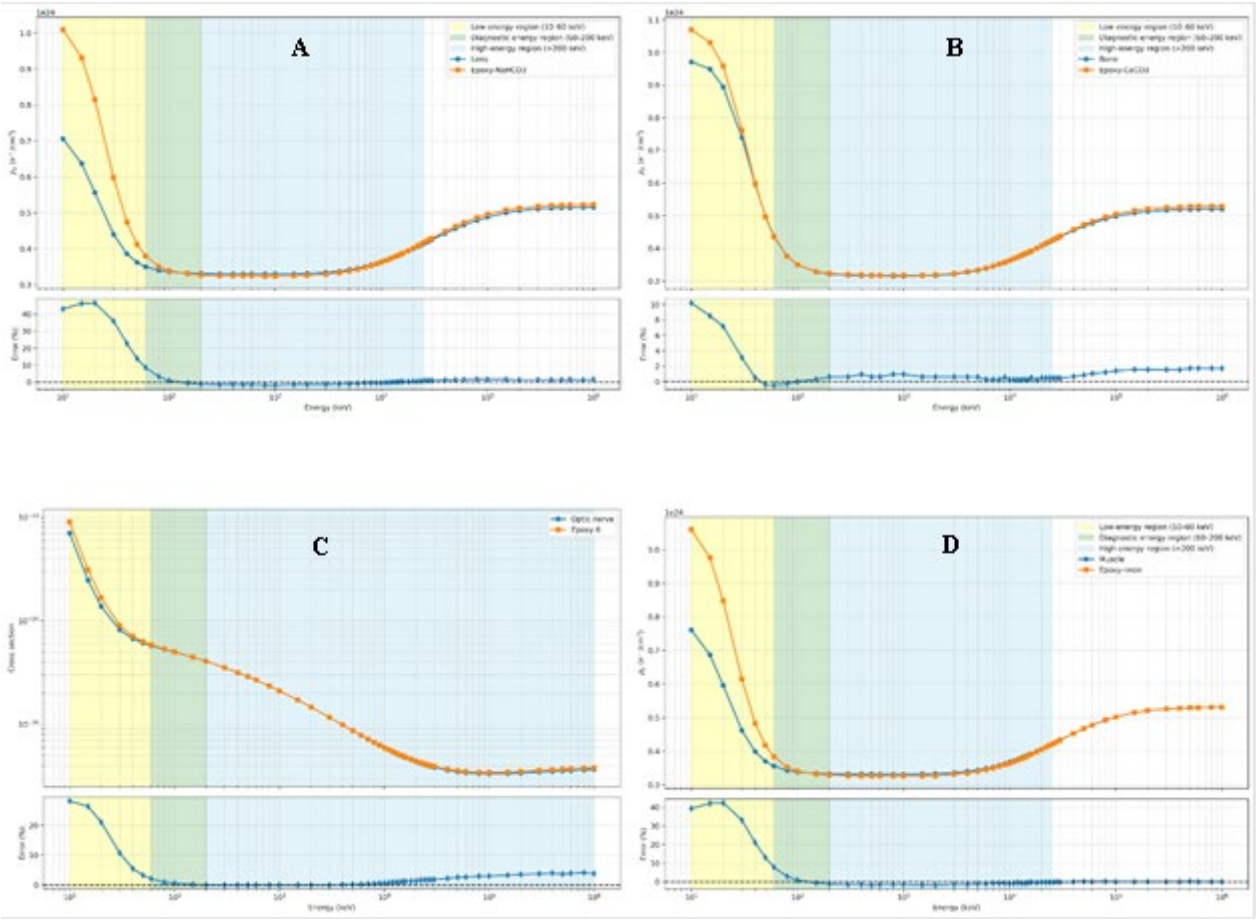

Figure 3: Energy-dependent electron density comparison for (**A**) crystalline lens, (**B**) orbital bone, (**C**) optic nerve, and (**D**) extraocular muscle tissue-equivalent materials. Lower panels show the relative deviations (%).

obtained trends stayed very close to those of the corresponding reference tissues, with low average deviations of approximately +0.8% for bone, +0.1% for the lens, −0.6% for muscle, and +1.5% for the optic nerve. These results confirm that the developed materials satisfactorily reproduce the electronic behavior of orbital tissues over the energy ranges relevant to dosimetry and radiation therapy applications.

Overall, the mass attenuation coefficient results demonstrated that the developed materials satisfactorily reproduced the radiological behavior of the corresponding reference orbital tissues over a wide energy range [Figure 4]. The largest deviations were observed at low energies, mainly below 60 keV, where photoelectric interactions dominate and remain strongly dependent on the atomic composition of the materials. In this energy region, the average deviations were approximately −8.7% for the Epoxy–$CaCO_3$ bone-equivalent composite, +52.3% for the Epoxy–$NaHCO_3$ lens-equivalent composite, +39% for the muscle-equivalent epoxy resin, and +34% for the Epoxy–acetone optic nerve–equivalent composite. Within the diagnostic energy range between 60 and 200 keV, the differences progressively decreased for all investigated materials, indicating improved agreement in the region dominated by Compton scattering. The average deviations in this range were approximately −1.2% for bone, +1.6% for the lens, −0.2% for muscle, and −0.3% for the optic nerve. At high energies between 200 keV and 25 MeV, the mass attenuation coefficients of the developed composites exhibited trends very close to those of the corresponding biological tissues, with relatively low and stable deviations. The average differences observed in this energy region were approximately −1.6% for bone, +0.09% for the lens, −1.0% for muscle, and −1.1% for the optic nerve. These results confirm the suitability of the developed materials for computed tomography, dosimetry, and radiation therapy applications involving orbital structures.

Table 2: Comparison of CT number values between human tissues and developed tissue-equivalent materials.

Tissue	Human Tissue (HU)	Tissue-Equivalent Material (HU)
Bone	601.7 ± 80	601.1 ± 60
Muscle	35.8 ± 4.8	36.0 ± 2.1
Optic nerve	34.9 ± 3.1	34.7 ± 2.0
Eye lens	65.9 ± 12.9	65.2 ± 6.8

The CT number analysis demonstrated a close agreement between the developed tissue-equivalent materials and the corresponding human orbital tissues [Table 2]. The orbital bone-equivalent material exhibited a mean CT number of 601.1±60 HU, which was comparable to the reference human bone value of 601.7±80 HU. Similarly, the muscle-equivalent material showed a CT number of 36.0±2.1 HU compared with 35.8±4.8 HU for human extraocular muscle tissue. The optic nerve–equivalent material presented a mean value of 34.7±2.0 HU, in agreement with the reference optic nerve

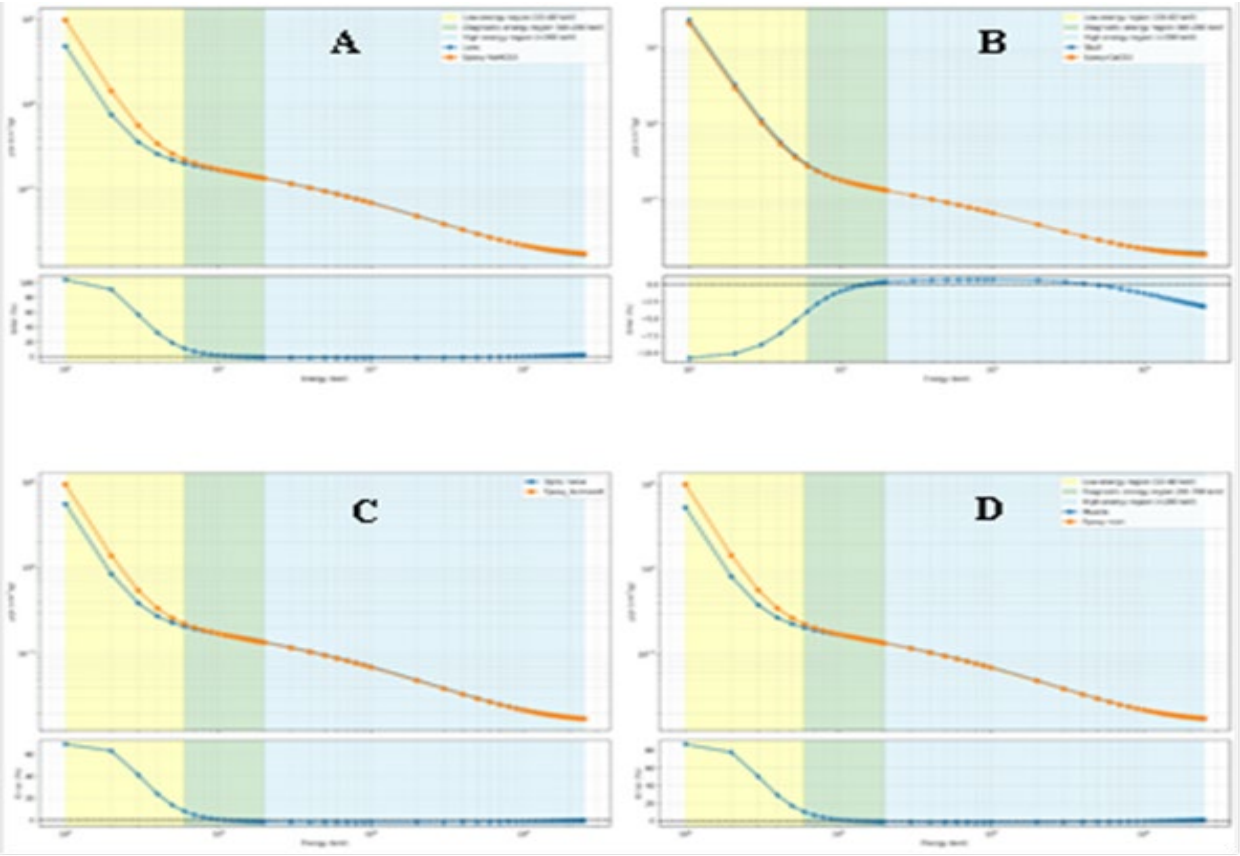

Figure 4: Energy-dependent mass attenuation coefficient (μ/ρ) comparison for (**A**) crystalline lens, (**B**) orbital bone, (**C**) optic nerve, and (**D**) extraocular muscle tissue-equivalent materials. Lower panels show the relative deviations (%).

value of 34.9±3.1 HU. For the crystalline lens, the developed Epoxy–$NaHCO_3$ composite produced a CT number of 65.2±6.8 HU, closely matching the corresponding human lens value of 65.9±12.9 HU. The limited differences observed for all investigated structures confirm the ability of the developed materials to reproduce the X-ray attenuation characteristics of orbital tissues under clinical computed tomography conditions, supporting their suitability for imaging, dosimetric, and radiation therapy applications.

DISCUSSION

The objective of this study was to develop and characterize epoxy-based tissue-equivalent materials capable of reproducing the radiological properties of the main orbital structures for computed tomography, dosimetric investigations, and radiation therapy applications. The obtained results demonstrated that the agreement between the developed materials and the corresponding biological tissues strongly depended on photon energy, reflecting the evolution of the dominant photon–matter interaction mechanisms.

At low energies below approximately 60 keV, the largest deviations were observed for both the effective atomic number Zeff and the mass attenuation coefficients μ/ρ. In this region, photon attenuation is mainly governed by the photoelectric effect [46], whose interaction probability strongly depends on both photon energy and atomic number, approximately proportional to Z^n/E^3 [47]. Consequently, relatively small differences in elemental composition between the developed composites and biological tissues may produce significant variations in attenuation behavior at low energies. This phenomenon was particularly observed for the Epoxy–$NaHCO_3$ lens-equivalent material and the muscle-equivalent epoxy resin, which exhibited higher mass attenuation coefficients than the corresponding biological tissues at low energies. The incorporation of sodium in the lens-equivalent material, as well as the intrinsic elemental composition of the epoxy matrix, contributed to increasing the effective atomic number of the composites, thereby enhancing photoelectric absorption. Similarly, the Epoxy–$CaCO_3$ bone-equivalent composite exhibited attenuation values close to those of the reference bone tissue because calcium increased the effective atomic number and improved the photoelectric interaction properties required for bone simulation [48]. The relationship observed between Zeff and the mass attenuation coefficients confirms the important role of atomic composition in low-energy attenuation processes [49]. Materials presenting effective atomic numbers close to those of the reference biological tissues generally exhibited lower deviations μ/ρ, particularly within the diagnostic energy range. This behavior highlights the importance of optimizing elemental composition during the development of tissue-equivalent materials intended to reproduce realistic radiological properties.

In the intermediate energy range between approximately 60 and 200 keV, corresponding to the spectrum typically used in clinical computed tomography [50], the differences between the developed materials and the reference tissues decreased

substantially. In this region, Compton scattering becomes the dominant interaction mechanism [51], and photon attenuation depends primarily on electron density rather than atomic number [43]. This explains the progressive convergence observed between the mass attenuation coefficient curves and the electron density values of the developed composites and the corresponding orbital tissues. The electron density results showed low average deviations in this energy range for all investigated materials, indicating that the developed composites reproduced the electronic environment of biological tissues with satisfactory accuracy. Consequently, the experimentally measured CT numbers also showed close agreement with those of the corresponding human tissues. Since CT numbers directly depend on the attenuation properties of materials under polyenergetic X-ray beams, this agreement confirms that the developed materials realistically reproduce tissue attenuation behavior under clinical imaging conditions. Furthermore, the low deviations observed despite beam-hardening effects indicate that the developed composites remain stable under realistic imaging conditions involving broad photon spectra rather than ideal monoenergetic beams.

At high energies above 200 keV and extending up to the megavoltage range used in radiation therapy, the developed materials also demonstrated stable radiological behavior. In this energy region, photon–matter interactions progressively evolve with an increasing contribution of pair production at very high energies [52]. In this domain, electron density and radiological interaction properties play a major role in photon transport and dose deposition [53]. The low deviations observed for electron density and mass attenuation coefficients indicate that the developed composites satisfactorily reproduce the physical interaction processes involved at high energies. This aspect is particularly important for orbital radiation therapy applications, where accurate dose estimation is required because of the high radiosensitivity of critical structures such as the crystalline lens and optic nerve. Overall, the agreement observed for effective atomic number, electron density, mass attenuation coefficients, and CT numbers confirms the radiological suitability of the developed epoxy-based composites for anthropomorphic orbital phantom fabrication. The obtained results demonstrate that the proposed materials can provide realistic attenuation and radiation transport properties over energy ranges relevant to CT-based dosimetry, and radiation therapy application.

CONCLUSION

This study enabled the development of a low-cost anthropomorphic orbital phantom based on epoxy resin tissue-equivalent materials for computed tomography and radiation therapy applications. The developed materials for orbital bone, extraocular muscles, optic nerve, and crystalline lens showed close agreement with the corresponding biological tissues in terms of effective atomic number, electron density, mass attenuation coefficients, and CT numbers over energy ranges relevant to both diagnostic imaging and high-energy radiotherapy applications. The obtained results confirm the ability of the proposed phantom to realistically reproduce the radiological properties of radiosensitive orbital structures, making it a relevant tool for medical imaging, CT protocol optimization, and dosimetric investigations.

Future perspectives include the integration of dosimetric detectors within the different orbital structures to evaluate dose distribution during CT examinations and radiation therapy procedures. Additional studies may also focus on dose assessment to the crystalline lens and optic nerve under different irradiation techniques, as well as on the optimization of imaging protocols and treatment plans aimed at reducing radiation exposure to critical orbital organs.

CREDIT AUTHORSHIP CONTRIBUTION STATEMENT

- **W. Allioui:** Writing-original draft, Conceptualization.
- **A. Khallouqi:** Investigation, Writing-review & editing.
- **H. Sekkat:** Investigation, Writing-review & editing.
- **A. Slimani:** Investigation, Writing-review & editing.
- **A. Halimi:** Writing-review & editing, Supervision, Methodology.
- **O. El rhazouani:** Writing-review & editing, Supervision.

DECLARATION OF COMPETING INTEREST

I hereby declare that I have no pecuniary or other personal interest, direct or indirect, in any matter that raises or may raise a conflict.

DATA AVAILABILITY

No data was used for the research described in the article.

ACKNOWLEDGMENTS

The authors would like to thank the Hassan 1st University Settat for the financial support.

REFERENCES

1. Jeganathan VSE, Wirth A, MacManus MP. Ocular Risks From Orbital and Periorbital Radiation Therapy: A Critical Review. Int J Radiat Oncol Biol Phys. 2011;79:650-659.
2. Demir H, Kanyilmaz G, Gul OV, Aksu T, Dastan Y, et al. Dosimetric comparison of radiotherapy techniques using TrueBeam, Halcyon, and helical tomotherapy in stage III NSCLC. Radiat Phys Chem. 2026;246:113964.
3. Shen J, An Y. Modern Radiotherapy for High-Risk and Very-High-Risk Prostate Adenocarcinoma. Urol Clin North Am. 2026;53:225-231.
4. Ainsbury EA, Barnard SGR. Sensitivity and latency of ionising radiation-induced cataract. Exp Eye Res. 2021;212:108772.
5. Nafchi ER, Fadavi P, Amiri S, Cheraghi S, Garousi M, et al. Radiomics model based on computed tomography images for prediction of radiation-induced optic neuropathy following radiotherapy of brain and head and neck tumors. Heliyon. 2025;11:e41409.
6. Ophthalmic complications of radiotherapy. Graefes Arch Clin Exp Ophthalmol. 2025.
7. Lederman M. Radiotherapy in the Treatment of Orbital Tumours. Br J Ophthalmol. 1956;40:592-610.
8. Hoffmans D, Nelissen K, Versteijne E, Verbakel W. Quality assurance of online adaptive radiotherapy workflows using film dosimetry in a 3D printed thorax anthropomorphic phantom. Phys Imaging Radiat Oncol. 2026;37:100909.
9. Li P, Fei XL, He PB, Shen X, Li Q, et al. Dosimetric verification on HIMM at the Wuwei heavy ion therapy center using anthropomorphic phantoms. Radiat Phys Chem. 2024;218:111644.
10. Bagahezel MS, Abdulkadir MK, Appalanaido GK, Mansor S, Abdul Razab MKA, et al. Radiological and Dosimetric Characteristics Evaluation of Enhanced 3D Printed Acrylonitrile Butadiene Styrene (ABS-Pro) as a Water-Equivalent Material (using radiotherapy treatment beam) in Radiotherapy Applications. Radiat Phys Chem. 2026:114007.
11. Kugel F, Schoroth F, Volkenborn V. PS07.28 ONLINE ADAPTIVE VS. CONVENTIONAL RADIATION THERAPY: A DOSIMETRIC STUDY USING 3D-PRINTED ANTHROPOMORPHIC PHANTOM. Phys Med. 2024;125:104180.
12. Sekkat H, Khallouqi A, Bannan A, El mouden O, El rhazouani O, et al. Validation of a cost-effective heterogeneous pediatric head phantom for CT-based HU-density calibration in radiotherapy treatment planning: A dosimetric evaluation in pediatric brain tumor cases. Radiat Phys Chem. 2025;237:113068.
13. Dierl M, Schönfeld AA, Casares-Magaz O, Bert C, Chofor N. Comprehensive quality assurance of a surface-guided radiotherapy system using a new anthropomorphic add-on phantom in a modular setup. Z Med Phys. 2025.
14. Santos WS, Xavier DAA, Santos CJ, Neves LP, Belinato W, et al. Dosimetric evaluation in brachytherapy and teletherapy for prostate cancer using Monte Carlo simulation and anatomically realistic virtual anthropomorphic phantom. Radiat Phys Chem. 2023;209:111000.
15. Craft DF, Howell RM. Preparation and fabrication of a full-scale, sagittal-sliced, 3D-printed, patient-specific radiotherapy phantom. J Appl Clin Med Phys. 2017;18:285-292.
16. Wu JK, Yu MC, Chen SH, Liao SH, Wang YJ. Low cost multifunctional 3D printed image quality and dose verification phantom for an image-guided radiotherapy system. PLoS One. 2022;17:e0266604.
17. Wood S, Krishnamurthy N, Santini T, Raval S, Farhat N, et al. Design and fabrication of a realistic anthropomorphic heterogeneous head phantom for MR purposes. PLoS One. 2017;12:e0183168.
18. Yin J, Li M, Dai G, Zhou H, Ma L, et al. 3D Printed Multi-material Medical Phantoms for Needle-tissue Interaction Modelling of Heterogeneous Structures. J Bionic Eng. 2021;18:346-360.
19. Vũ Bezin J, Allodji RS, Mège JP, Beldjoudi G, Saunier F, et al. A review of uncertainties in radiotherapy dose reconstruction and their impacts on dose–response relationships. J Radiol Prot. 2017;37:R1.
20. Yadav N, Singh M, Mishra SP. Tissue-equivalent materials used to develop phantoms in radiation dosimetry: A review. Mater Today Proc. 2021;47:7170-7173.
21. Huamani T Y, Mullisaca P A, Apaza V G, Chen F, Vega R J. Construction and characterization of materials equivalent to the tissues and organs of the human body for radiotherapy. Radiat Phys Chem. 2019;159:70-75.
22. Cook H, Simard M, Niemann N, Gillies C, Osborne M, et al. Development of optimised tissue-equivalent materials for proton therapy. Phys Med Biol. 2023;68:075009.
23. Choi Y, Jang YJ, Kim KB, Bahng J, Choi SH. Characterization of Tissue Equivalent Materials Using 3D Printing for Patient-Specific DQA in Radiation Therapy. Appl Sci. 2022;12:9768.
24. Kucuk N, Cakir M, Isitman NA. Mass attenuation coefficients, effective atomic numbers and effective electron densities for some polymers. Radiat Prot Dosimetry. 2013;153:127-134.
25. Al-Buriahi MS, Tonguc BT. Mass attenuation coefficients, effective atomic numbers and electron densities of some contrast agents for computed tomography. Radiat Phys Chem. 2020;166:108507.
26. Kore PS, Pawar PP. Measurements of mass attenuation coefficient, effective atomic number and electron density of some amino acids. Radiat Phys Chem. 2014;98:86-91.
27. Badiuk SR, Sasaki DK, Rickey DW. An anthropomorphic maxillofacial phantom using 3-dimensional printing, polyurethane rubber and epoxy resin for dental imaging and dosimetry. Dentomaxillofac Radiol. 2022;51:20200323.
28. Demirel SZ, Yücel H. Development of a novel paediatric anthropomorphic phantom from epoxy based mixtures for 5 year age child bone tissue equivalency. Radiat Phys Chem. 2026;238:113209.
29. Winslow JF, Hyer DE, Fisher RF, Tien CJ, Hintenlang DE. Construction of anthropomorphic phantoms for use in dosimetry studies. J Appl Clin Med Phys. 2009;10:195-204.
30. Alanqari K, Al-Yami A, Wagle V, Al-Jubran M. Innovative Epoxy Resin Formulation. IPTC Proceedings. n.d.
31. Bello S, Agunsoye J, Hassan B, Zebaze Kana M, Raheem I. Epoxy Resin Based Composites, Mechanical and Tribological Properties: A Review. Tribol Ind. 2015;37.
32. Gonçalves FAMM, Santos M, Cernadas T, Alves P, Ferreira P. Influence of fillers on epoxy resins properties: a review. J Mater Sci. 2022;57:15183-15212.
33. Khallouqi A, Halimi A, El Rhazouani O, Mesradi MR, El Mansouri K, et al. Comparing tissue-equivalent properties of polyester and epoxy resins with PMMA material using Gate/Geant4 simulation toolkit. Radiat Phys Chem. 2024;220:111702.
34. Carton AK, Bakic P, Ullberg C, Derand H, Maidment ADA. Development of a physical 3D anthropomorphic breast phantom. Med Phys. 2011;38:891-896.
35. Gear JI, Cummings C, Craig AJ, Divoli A, Long CDC, et al. Abdo-Man: a 3D-printed anthropomorphic phantom for validating quantitative SIRT. EJNMMI Phys. 2016;3:17.
36. Zhang F, Zhang H, Zhao H, He Z, Shi L, et al. Design and fabrication of a personalized anthropomorphic phantom using 3D printing and tissue equivalent materials. Quant Imaging Med Surg. 2019;9:94-100.
37. Jahnke P, Schwarz FB, Ziegert M, Almasi T, Abdelhadi O, et al. A radiopaque 3D printed, anthropomorphic phantom for simulation of CT-guided procedures. Eur Radiol. 2018;28:4818-4823.

38. Karimi M, Mostaghimi H, Shams SF, Mehdizadeh AR. Design and Production of Two-piece Thyroid-neck Phantom by the Concurrent Use of Epoxy Resin and Poly(methyl methacrylate) Soft Tissue Equivalent Materials. J Biomed Phys Eng. 2018;8:217-222.
39. Caldas MP, Ramos-Perez FMM, Almeida SM, Haiter-Neto F. Comparative evaluation among different materials to replace soft tissue in oral radiology studies. J Appl Oral Sci. 2010;18:264-267.
40. Lehnert AL, Hunter WCJ, McDougald WA, Harrison RL, Lewellen TK, et al. Development and testing of SPECT/CT lung phantoms made from expanding polyurethane foam. Med Phys. 2019;46:5593-5601.
41. Valentin J. Basic anatomical and physiological data for use in radiological protection: reference values: ICRP Publication 89. Ann ICRP. 2002;32:1-277.
42. Eritenko AN, Tsvetyansky AL, Polev AA. Coefficients d' atténuation massique et numéros atomiques effectifs de $Gd_3Al_2Ga_3O_{12}$: Ce et $CaMoO_4$ dans la gamme d'énergie 30–662 keV. Nucl Instrum Methods Phys Res B. 2026;570:165914.
43. Bouchard-Gilanton V. Modélisation et correction de l'effet Compton dans la reconstruction d'images tomoscintigraphiques. Thesis. 1997.
44. Amako K, Guatelli S, Ivanchenko VN, Maire M, Mascialino B, et al. Comparison of Geant4 electromagnetic physics models against the NIST reference data. IEEE Trans Nucl Sci. 2005;52:910-918.
45. Evans RD. Compton Effect. In: Corpuscles and Radiation in Matter II / Korpuskeln Und Strahlung in Materie II. 1958:218-298.
46. Pratt RH, Ron A, Tseng HK. Atomic Photoelectric Effect Above 10 keV. Rev Mod Phys. 1973;45:273-325.
47. Wirawan R, Qomariyah N, Ardianto T, Kurniawidi DW. Radiation shielding potential analyze of iron sand-pumice composite based on GEANT4 simulations. AIP Conf Proc. 2023;2619:050013.
48. Zhu K, Prince RL. Calcium and bone. Clin Biochem. 2012;45:936-942.
49. Amin NAB, Zukhi J, Kabir NA, Zainon R. Determination of effective atomic numbers from mass attenuation coefficients of tissue-equivalent materials in the energy range 60 keV-1.33 MeV. J Phys Conf Ser. 2017;851:012018.
50. Nazemi E, Six N, Iuso D, De Samber B, Sijbers J, et al. Monte-Carlo-Based Estimation of the X-ray Energy Spectrum for CT Artifact Reduction. Appl Sci. 2021;11:3145.
51. McCullough EC. Photon attenuation in computed tomography. Med Phys. 1975;2:307-320.
52. Djamaa N, Tebboub W, Boukhellout A. Simulation par la méthode Monte Carlo d'un accélérateur linéaire médical en radiothérapie. Thesis. 2020.
53. Barateau A, Céleste M, Lafond C, Henry O, Couespel S, et al. Calcul de dose de radiothérapie à partir de tomographies coniques : état de l'art. Cancer Radiother. 2018;22:85-100.